Supporting Information

Structural characterization and quantitation of ether-linked glycerophospholipids in peroxisome biogenesis disorder tissue by ultraviolet photodissociation mass spectrometry

Molly S. Blevins[1,±], Samuel W. J. Shields[1,±], Wei Cui[2], Wedad Fallatah[3,5], Ann B. Moser[6,7], Nancy E. Braverman[2,3,4], Jennifer S. Brodbelt[1,*]

[1]Department of Chemistry, University of Texas at Austin, Austin, TX 78712, United States

[2]Research Institute of the McGill University Health Center, [3]Department of Human Genetics, [4]Department of Pediatrics, McGill University and the, Montreal, Quebec HA 0C7, Canada

[5]Department of Medical Genetics, King Abdul-Aziz University, Jeddah, Saudi Arabia

[6]Kennedy Krieger Institute, Baltimore, MD 21205, United States

[7]School of Medicine, Johns Hopkins University, Baltimore, MD 21205, United States

[±]These authors contributed equally. *correspondence to: jbrodbelt@cm.utexas.edu

Figure S1. Positive-mode HCD mass spectra of singly protonated ether glycerophospholipid standards **(a)** PC(*O*-16:0/18:1(9Z)), **(b)** PE(*O*-16:0/18:1(9Z)), **(c)** PC(*P*-18:0/18:1(9Z)), and **(d)** PE(*P*-18:0/18:1(9Z)) with corresponding fragment maps **(e-h)**.

(a) PC(*O*-16:0/18:1(9*Z*)), $[M+H]^+$ = *m/z* 746.6

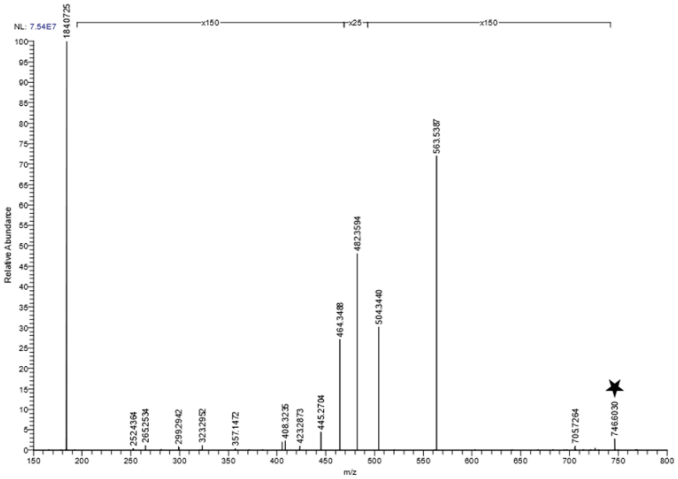

(b) PE(*O*-16:0/18:1(9*Z*)), $[M+H]^+$ = *m/z* 704.6

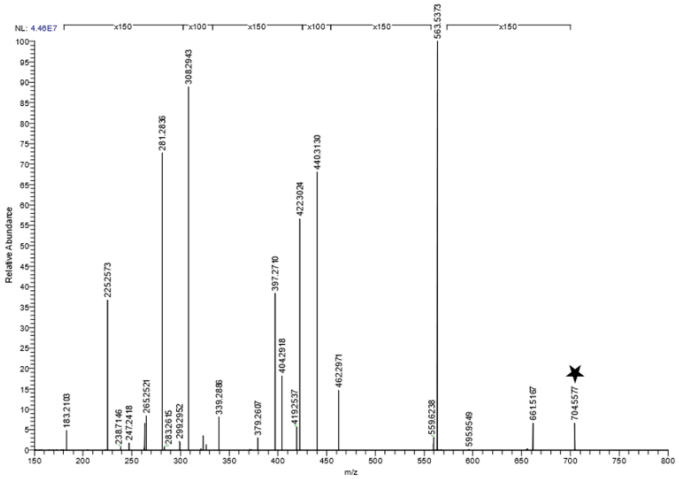

(c) PC(*P*-18:0/18:1(9*Z*)), $[M+H]^+$ = *m/z* 772.6

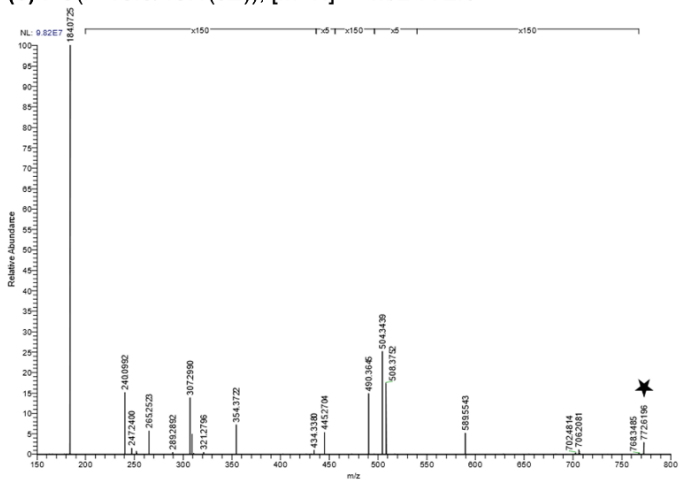

(d) PE(*P*-18:0/18:1(9*Z*)), $[M+H]^+$ = *m/z* 730.5

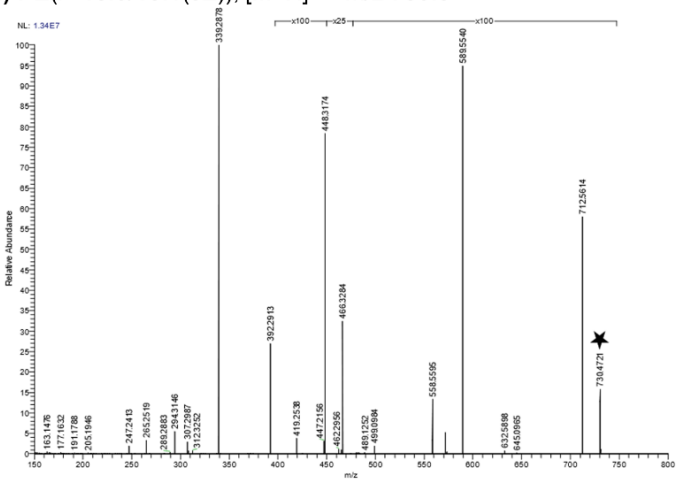

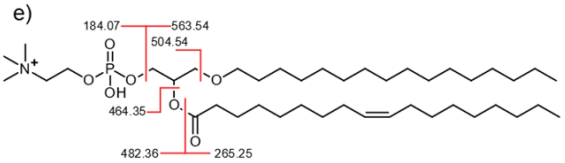

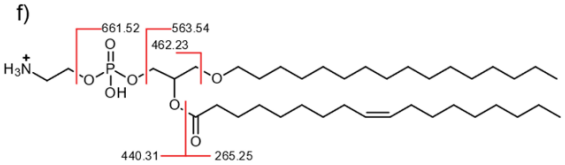

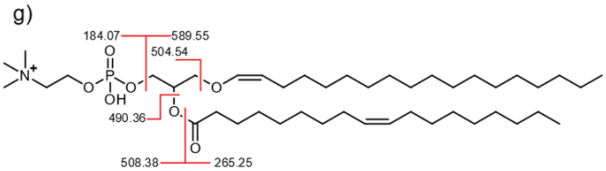

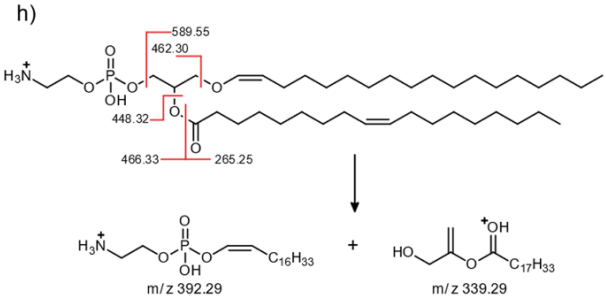

Figure S2. Negative-mode HCD mass spectra of singly deprotonated ether glycerophospholipid standards **(a)** PC(*O*-16:0/18:1(9*Z*)), **(b)** PE(*O*-16:0/18:1(9*Z*)), **(c)** PC(*P*-18:0/18:1(9*Z*)), and **(d)** PE(*P*-18:0/18:1(9*Z*)) with corresponding fragment maps **(e-h)**.

(a) PC(*O*-16:0/18:1(9*Z*)), $[M-H+CO_2H]^-$ = *m/z* 790.6

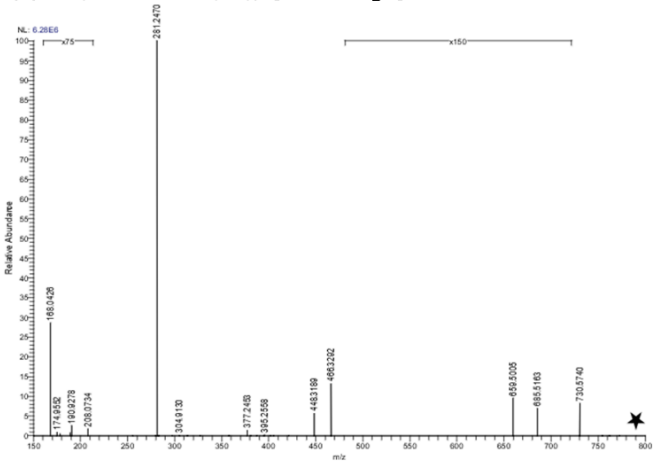

(b) PE(*O*-16:0/18:1(9*Z*)), $[M-H]^-$ = *m/z* 702.6

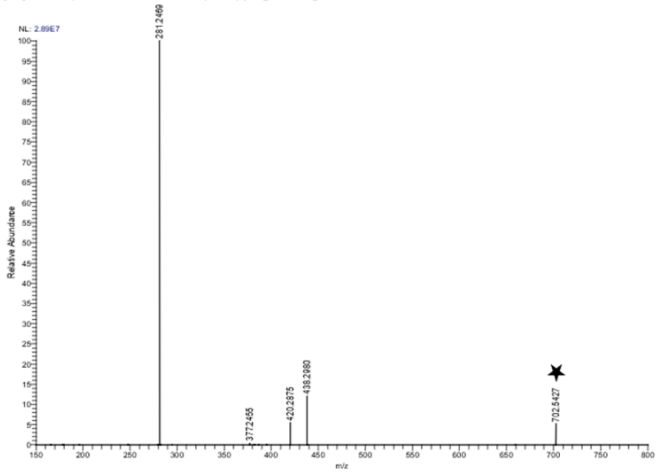

(c) PC(*P*-18:0/18:1(9*Z*)), $[M-H+CO_2H]^-$ = *m/z* 816.6

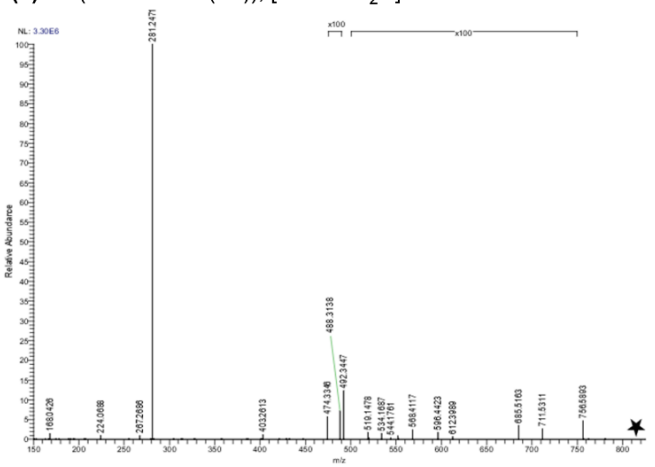

(d) PE(*P*-18:0/18:1(9*Z*)), $[M-H]^-$ = *m/z* 728.5

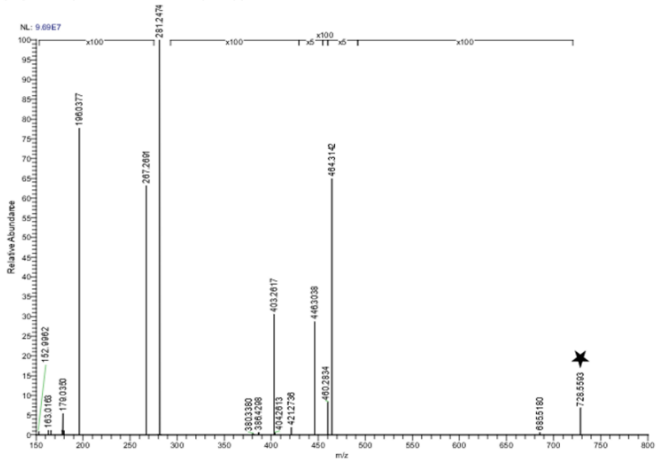

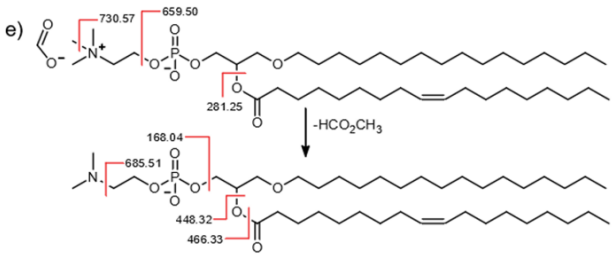

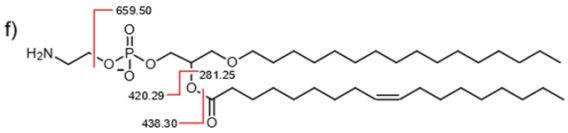

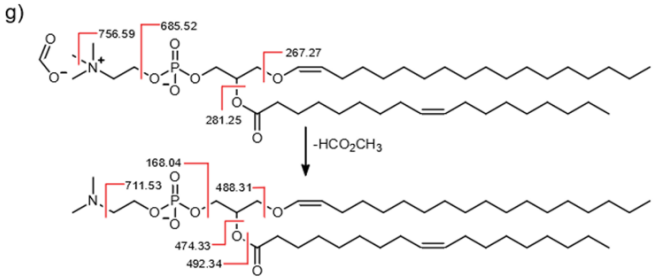

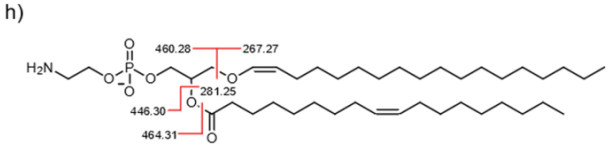

Figure S3. (a-h) Negative-mode 213 nm UVPD mass spectra of singly deprotonated ether glycerophospholipid standards **(a)** PC(*O*-16:0/18:1(9*Z*)), **(b)** PE(*O*-16:0/18:1(9*Z*)), **(c)** PC(*P*-18:0/18:1(9*Z*)), and **(d)** PE(*P*-18:0/18:1(9*Z*)) with corresponding fragment maps **(e-h)**.

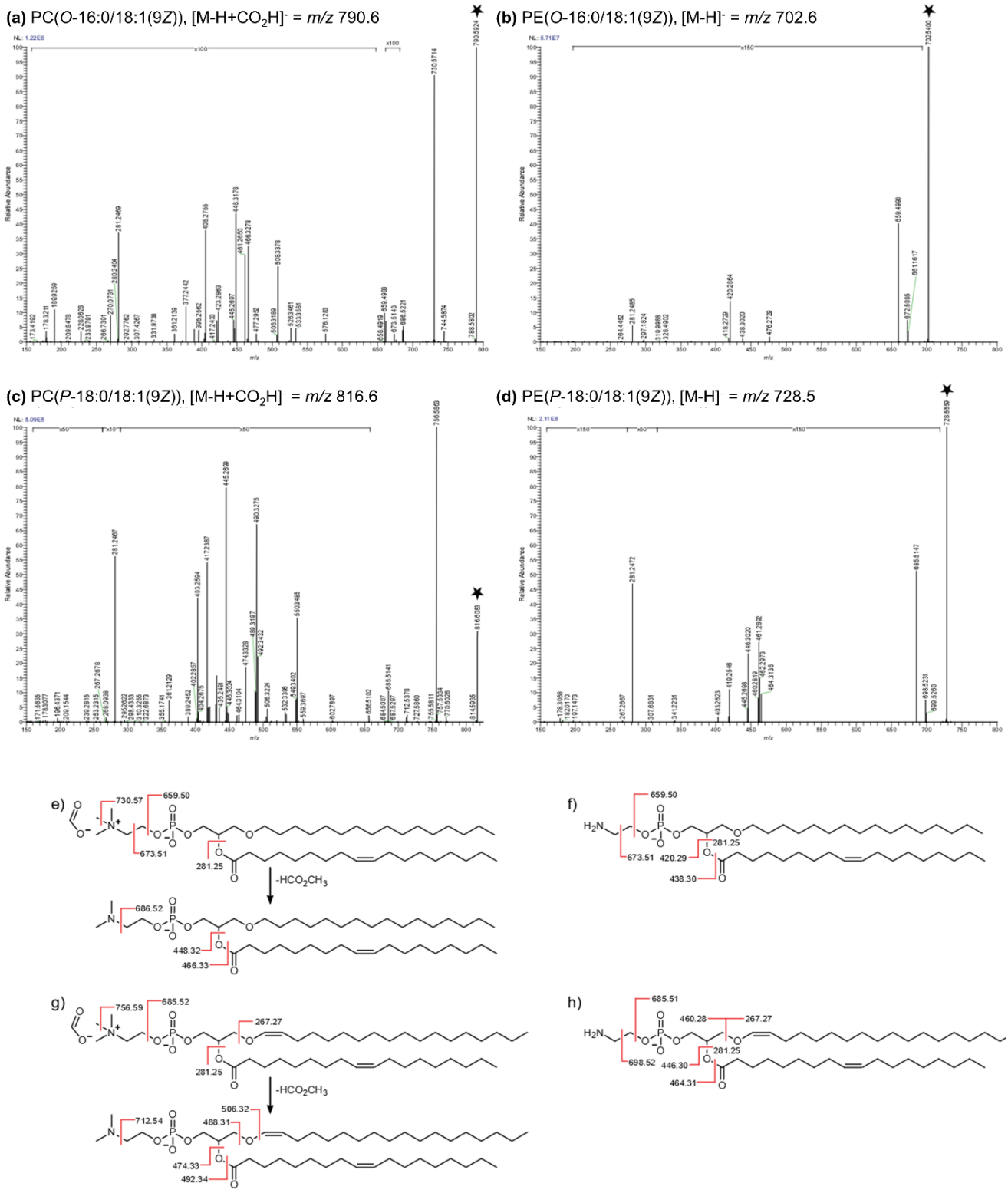

Figure S4. Positive-mode RPLC-MS base peak trace (in black) of 6-lipid mixture with colored XICs. All XICs are displayed with 20 ppm error tolerances on selected XIC *m/z* values. For the three PEs, the standard ester-linkage PE elutes first (PE(16:0/18:1(9*Z*)), RT 25.5 min), followed by the plasmanyl PE (PE(*O*-16:0/18:1(9*Z*)), RT 29.2 min), and finally the plasmenyl PE (PE(*P*-18:0/18:1(9*Z*)), RT 34.6 min). For the three PC lipids, the plasmanyl PC elutes first (PC(*O*-16:0/18:1(9*Z*)), RT 27.5 min), followed by the regular ester-linked PC (PC(18:0/18:1(9*Z*)), RT 29.9 min), and finally the plasmenyl PC (PC(*P*-18:0/18:1(9*Z*)), RT 32.7 min). For lipids with identical *sn*-1 and *sn*-2 chain compositions, differing only in sn-1 linkage type (regular-ester, ether, vinyl ether), some general features of the order of elution are apparent. The plasmenyl lipids are retained longer than the ester-linked counterparts (PC(*P*-18:0/18:1(9*Z*)), RT 32.7 min vs. PC(18:0/18:1(9*Z*)), RT 29.9 min; ΔRT 2.8 min). This characteristic shift in retention time caused by the vinyl ether moiety is distinct from the shift in retention time attributed to the presence of a C=C double bond within the alkyl chain. Similarly, plasmanyl lipids also are retained more strongly than ester-linked lipids (PE(*O*-16:0/18:1(9*Z*)), RT 29.2 min vs. PE(16:0/18:1(9*Z*)), RT 25.5 min; ΔRT 3.7 min). PCs are known to elute earlier than PE lipids owing to the presence of the three extra methyl groups on the nitrogen atom of the headgroup, effectively increasing the headgroup polarity and diminishing their interactions with the non-polar stationary phase.

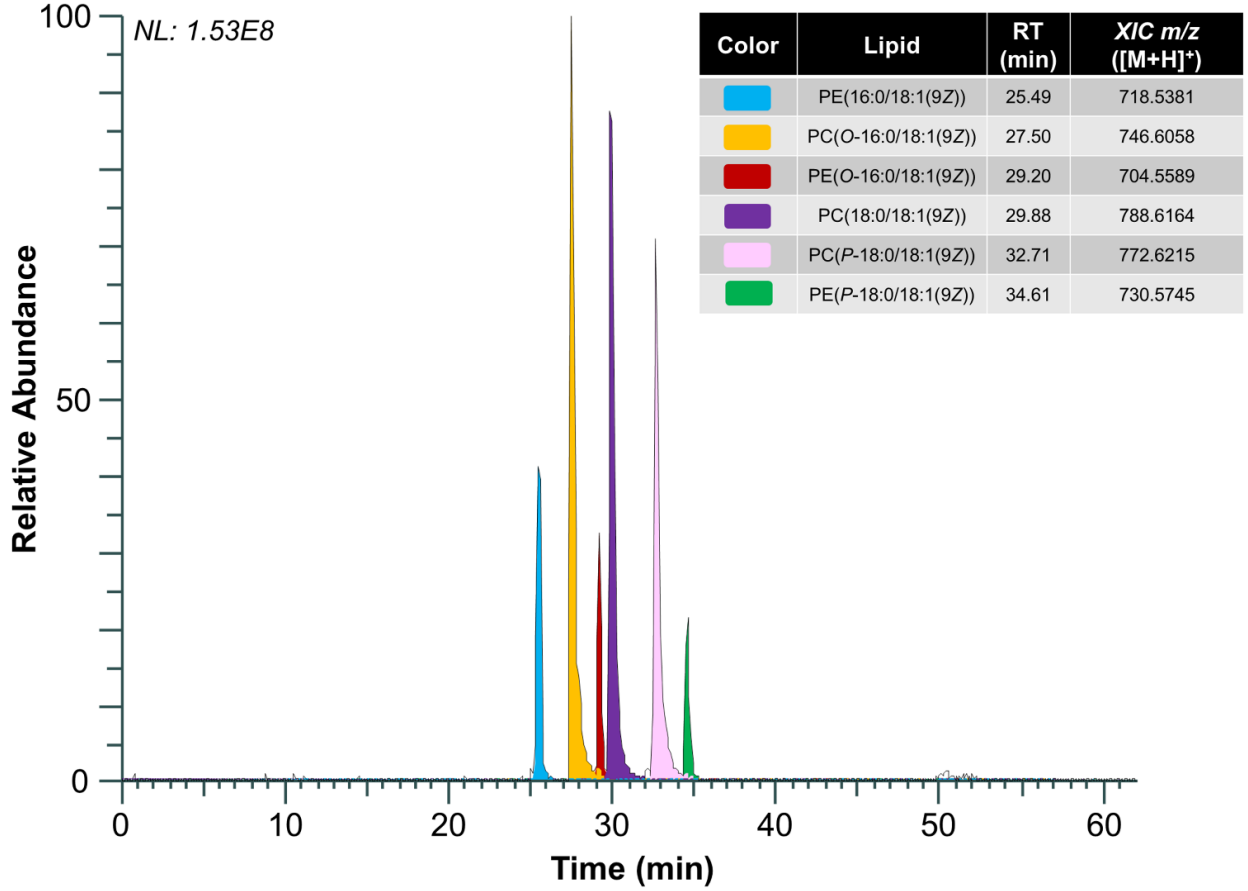

Figure S5. (a) XICs from positive-mode RPLC of one set of injections of internal standards PE(*P*-18:0/18:1-d_9(9*Z*)) and PC(*P*-16:0/16:0-d_9) ranging from 0.39-100 pmol per lipid per injection, **(b)** calibration curve of internal standards with LOD and LOQ values listed. All XICs are displayed with 20 ppm error tolerances on selected XIC *m/z* values. Linear regression and determination of the slope and intercept values for these two data sets enabled determination of both limit of detection (LOD) and limit of quantitation (LOQ).

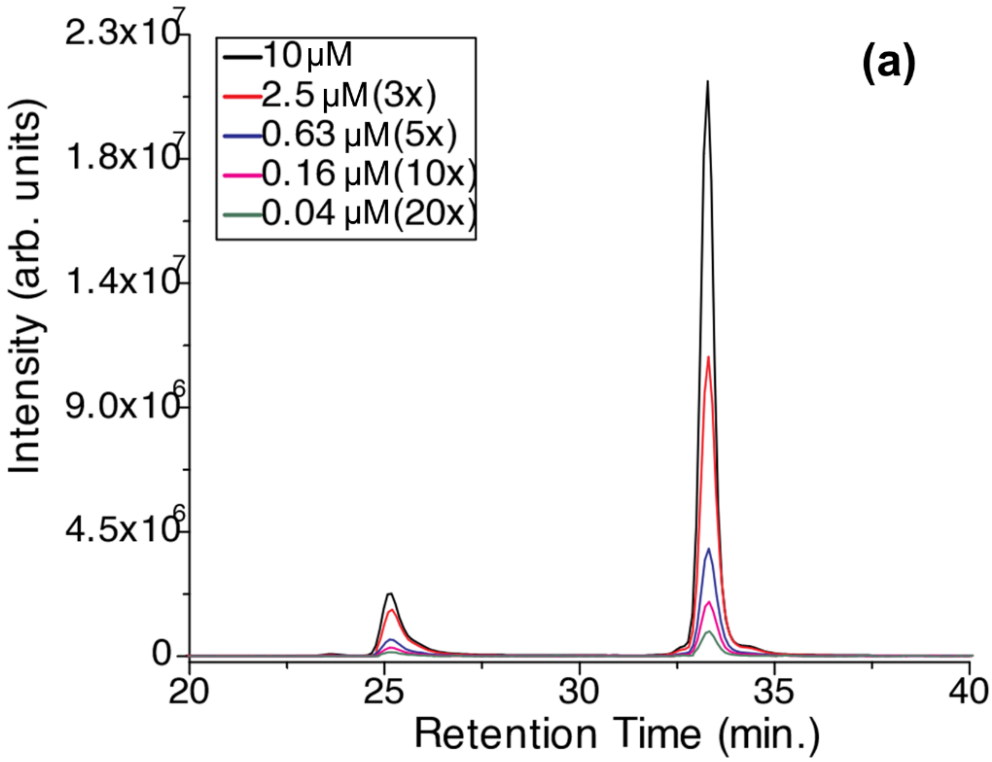

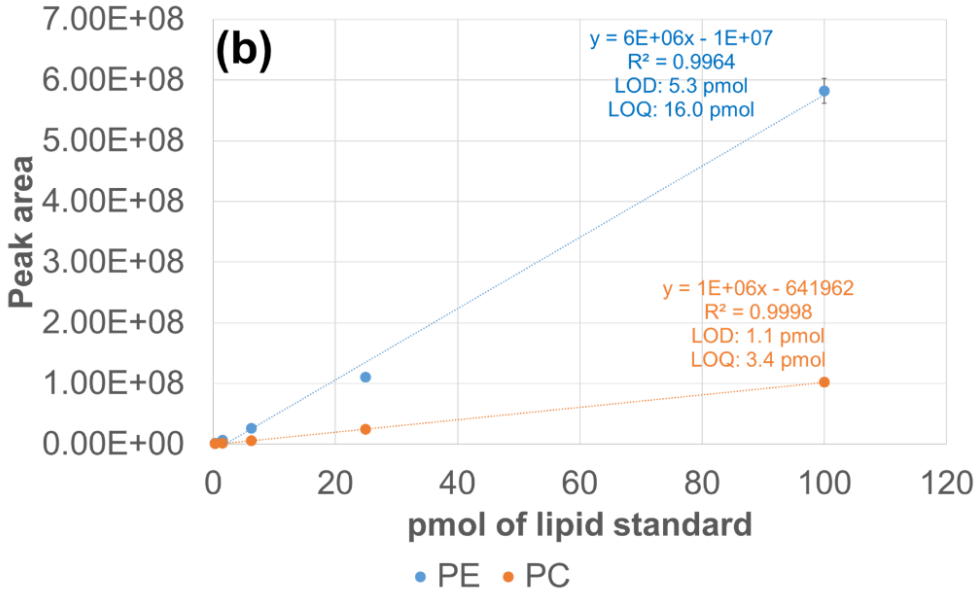

Figure S6. (a) Example of base peak LCMS trace of one run of mouse tissue (cerebellum C5 tissue sample, genotype HT) with XICs of lipid targets from negative-mode HCD data along with accompanying table displaying Lipid ID, retention time, and XIC *m/z*, **(b)** Representative HCD mass spectrum for lipid target of *m/z* 774.54 identified as PE(*P*-18:0/22:6) at RT 26.9 min with corresponding fragment map, and **(c)** fragment map with corresponding HCD ions which are critical for ether lipid identification. The critical fragment ions required for identification of ether linkage type and acyl chain identification are bolded. All XICs are displayed with 20 ppm error tolerances on selected XIC *m/z* values, while RT values listed in the table corresponding to HCD scan RT values at which the given precursors were identified. The automated LipiDex identification uses the *m/z* value of the precursor along with the *sn*-2 acyl chain product ion of *m/z* 327 to identify the lipid; however auxiliary interpretation of the spectrum is necessary to confirm whether the lipid is a plasmanyl or plasmenyl PE. Manual curation of the MS/MS spectrum identifies two low-abundance but important ions of *m/z* 267 and 506. These complementary ions correspond to cleavage at the C-O bond of the vinyl ether which is closest to the glycerol backbone, thus validating this ether lipid as PE(*P*-18:0/22:6) (and not the isomeric alternative lipid PE(*O*-18:1/22:6)). The MS/MS spectrum also shows the appearance of a fragment ion of *m/z* 283.2405, which does not mirror the cleavage patterns observed for the four standard ether lipids. This ion is attributed to the loss of CO_2 from the *sn*-2 acyl chain product ion of *m/z* 327.2303.

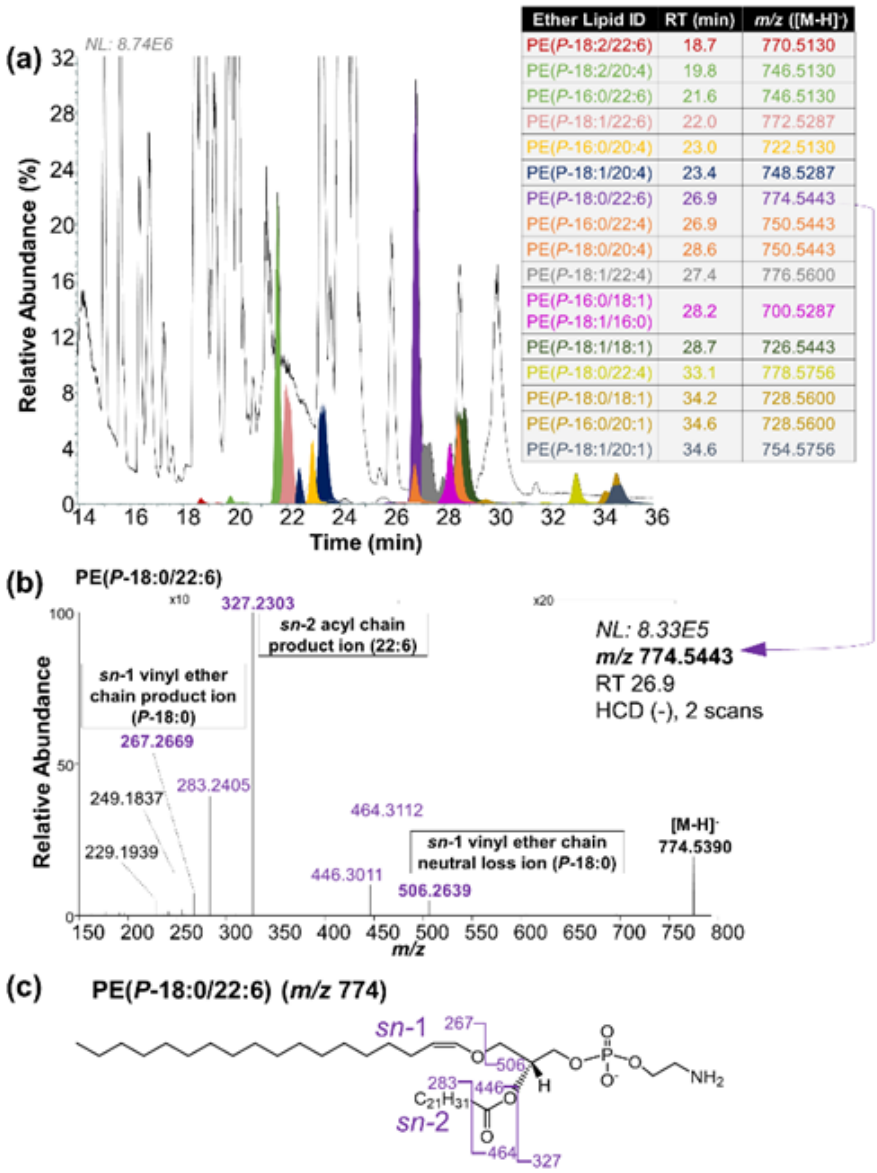

Figure S7. Base peak LC-MS traces from untargeted negative-mode HCD analysis of all mouse cerebellum lipid extracts.

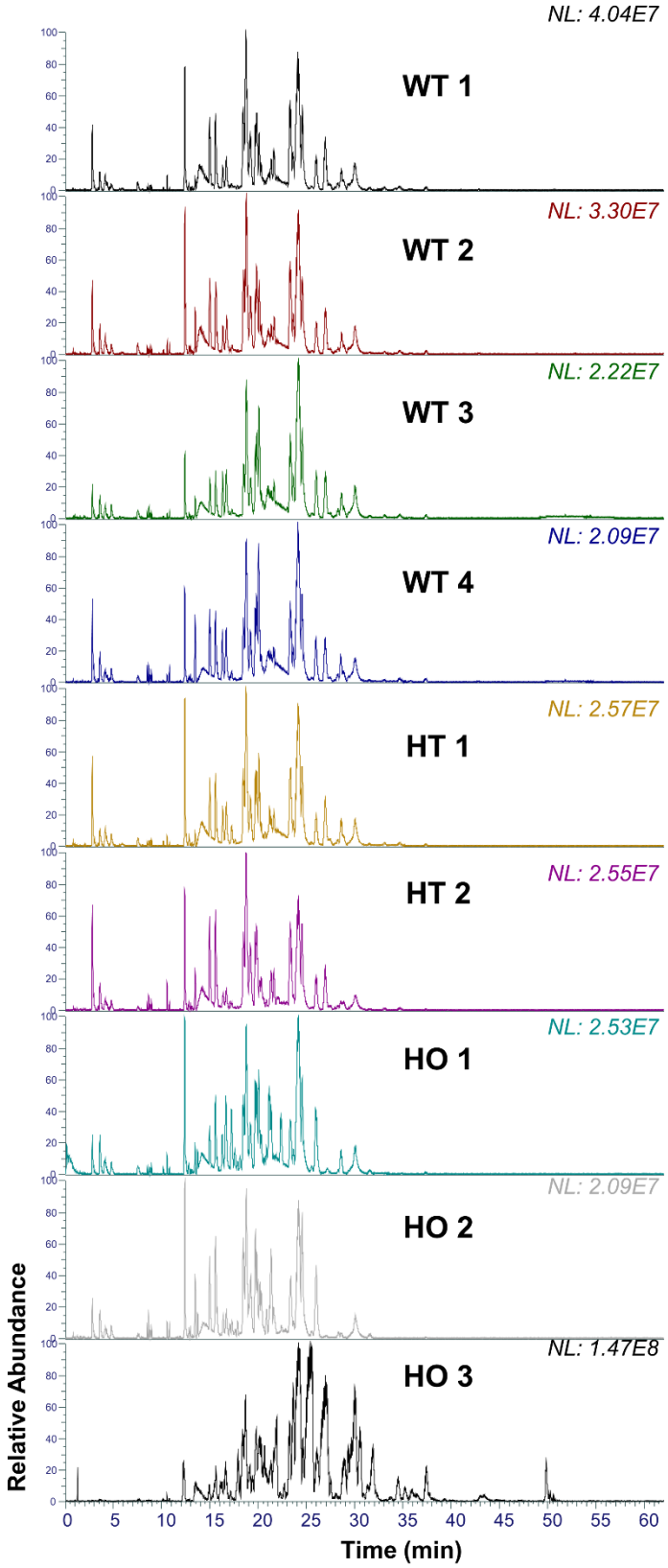

Figure S8. Base peak LC-MS traces from untargeted negative-mode HCD analysis of all mouse hippocampus lipid extracts.

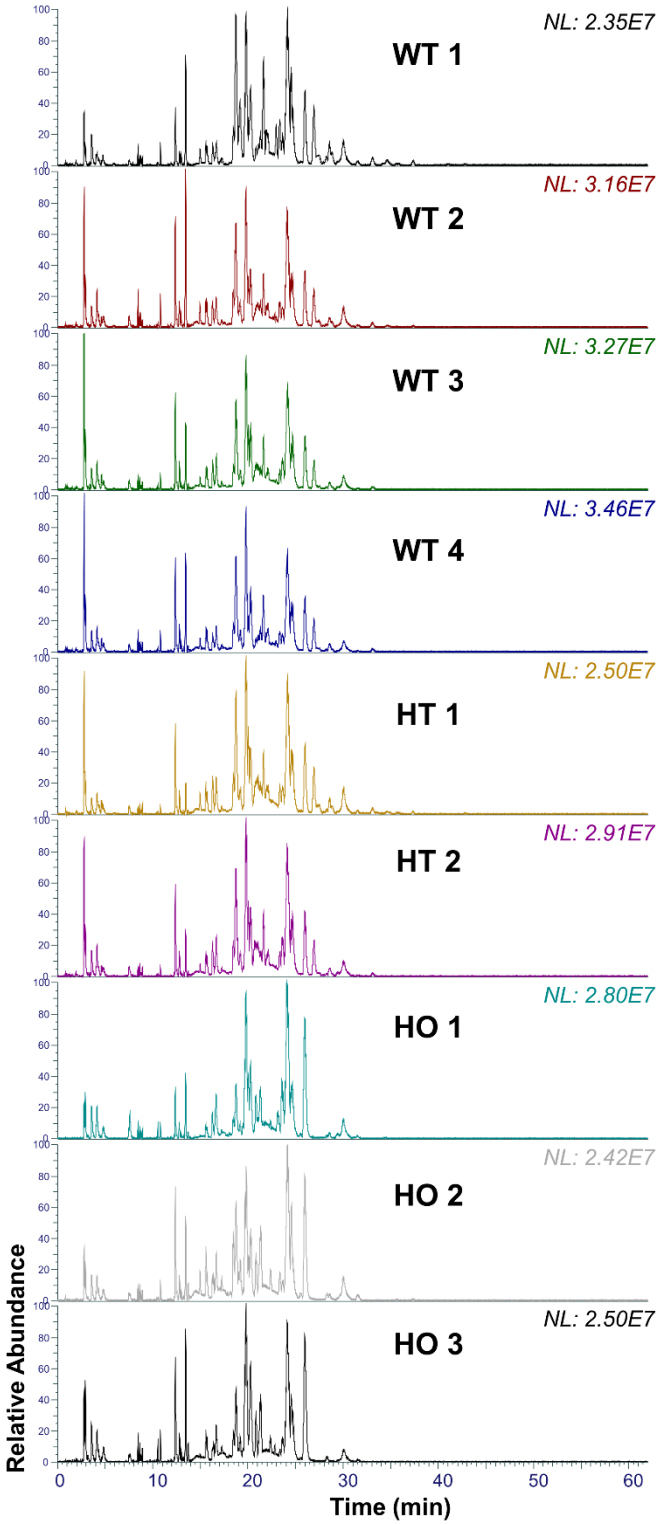

Figure S9. Base peak LC-MS traces from untargeted negative-mode HCD analysis of all mouse cortex lipid extracts.

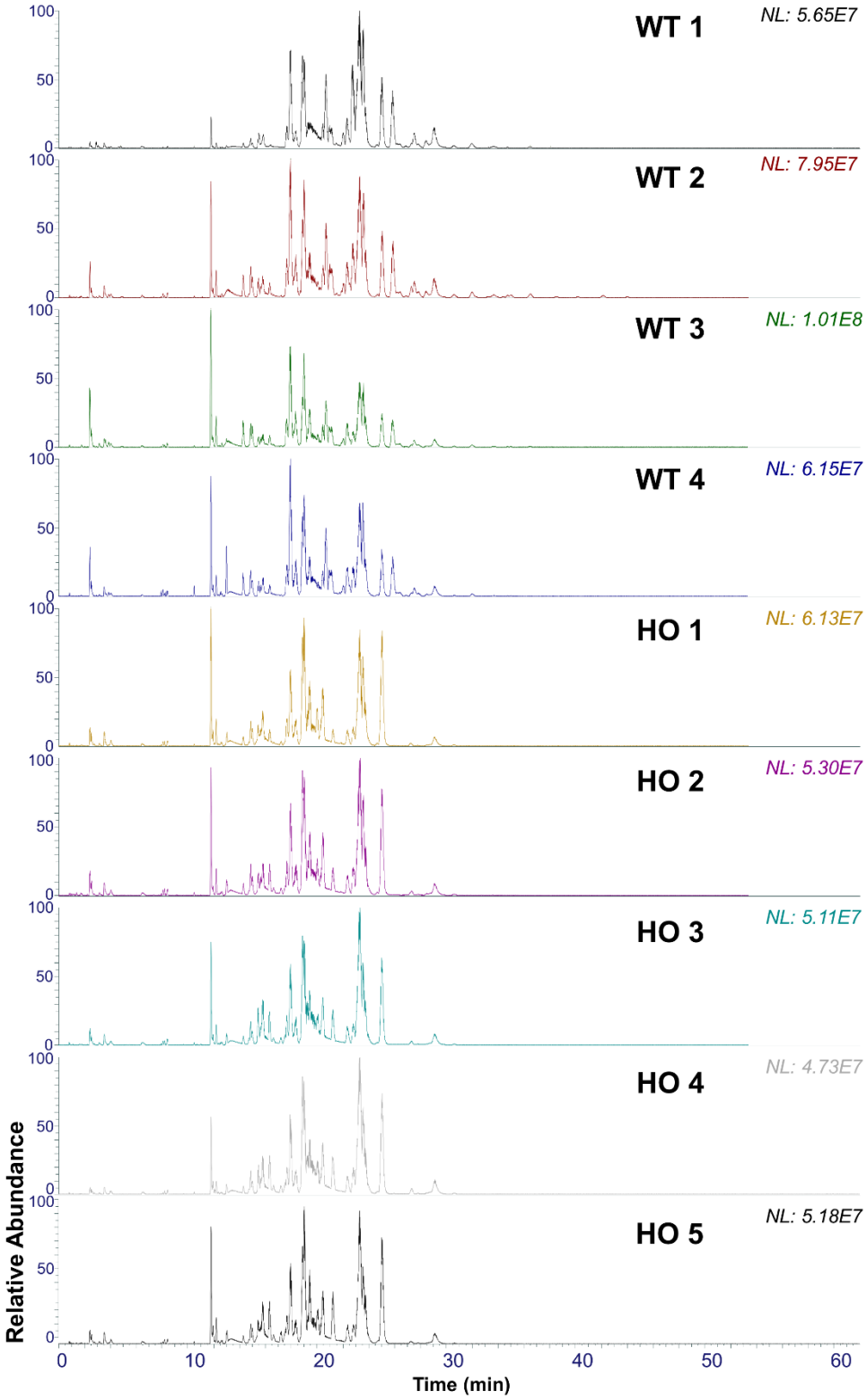

Figure S10. Base peak LC-MS traces from targeted positive-mode UVPD analysis of all mouse cerebellum lipid extracts.

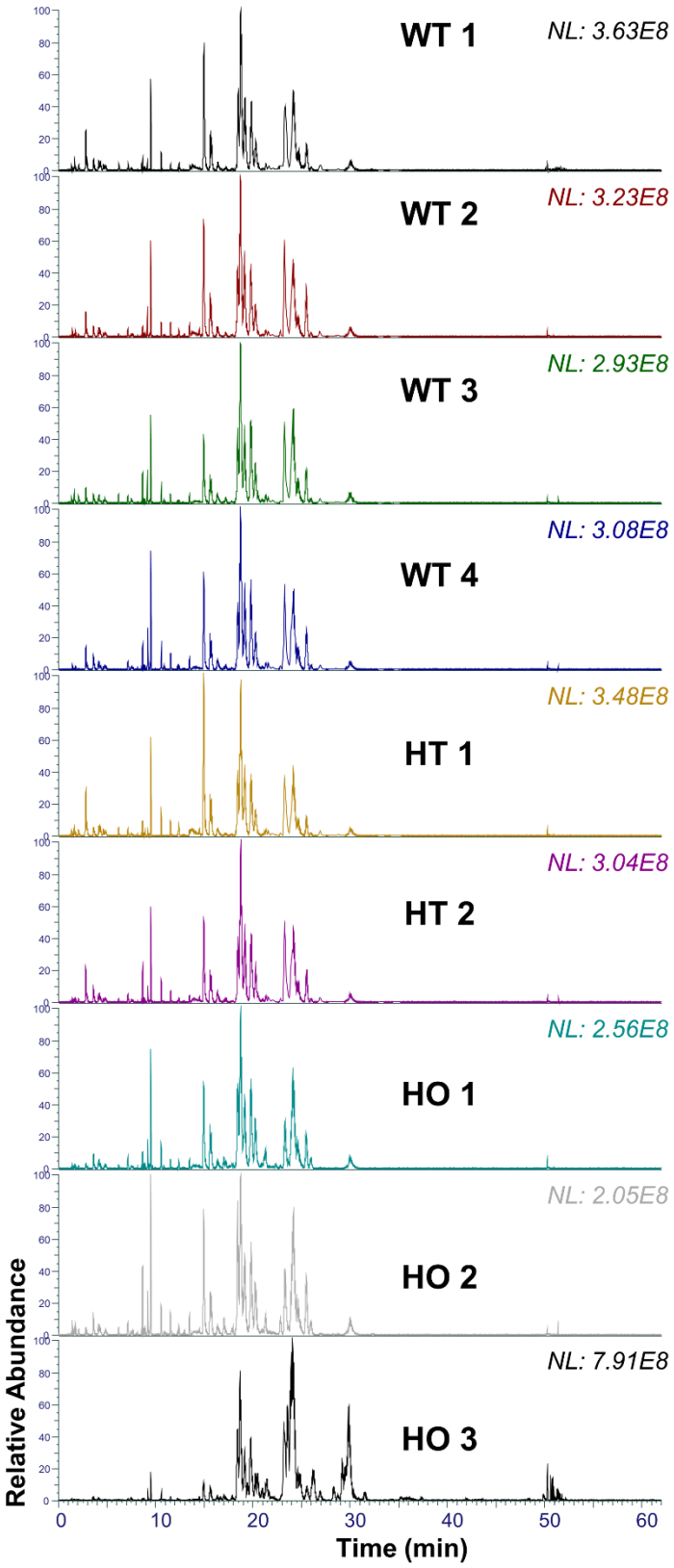

Figure S11. Base peak LC-MS traces from targeted positive-mode UVPD analysis of all mouse hippocampus lipid extracts.

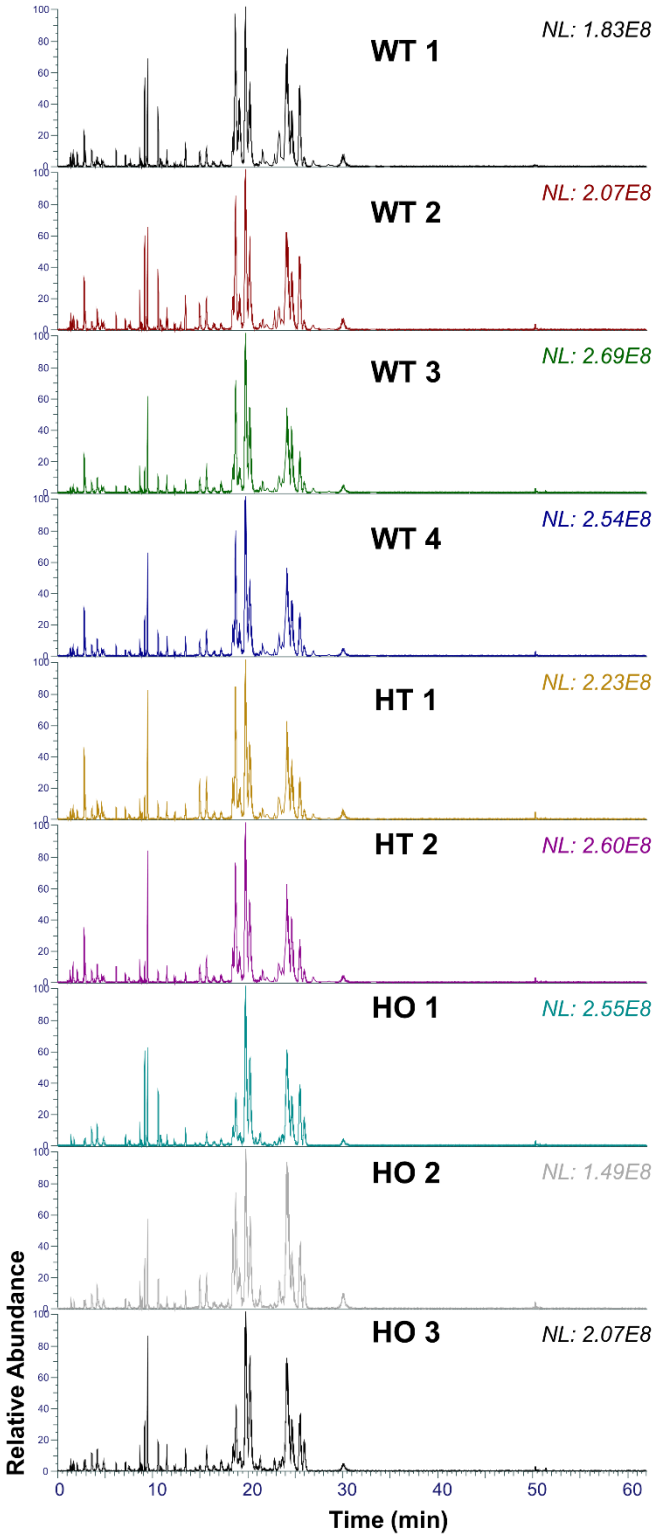

Figure S12. Base peak LC-MS traces from targeted positive-mode UVPD analysis of all mouse cortex lipid extracts.

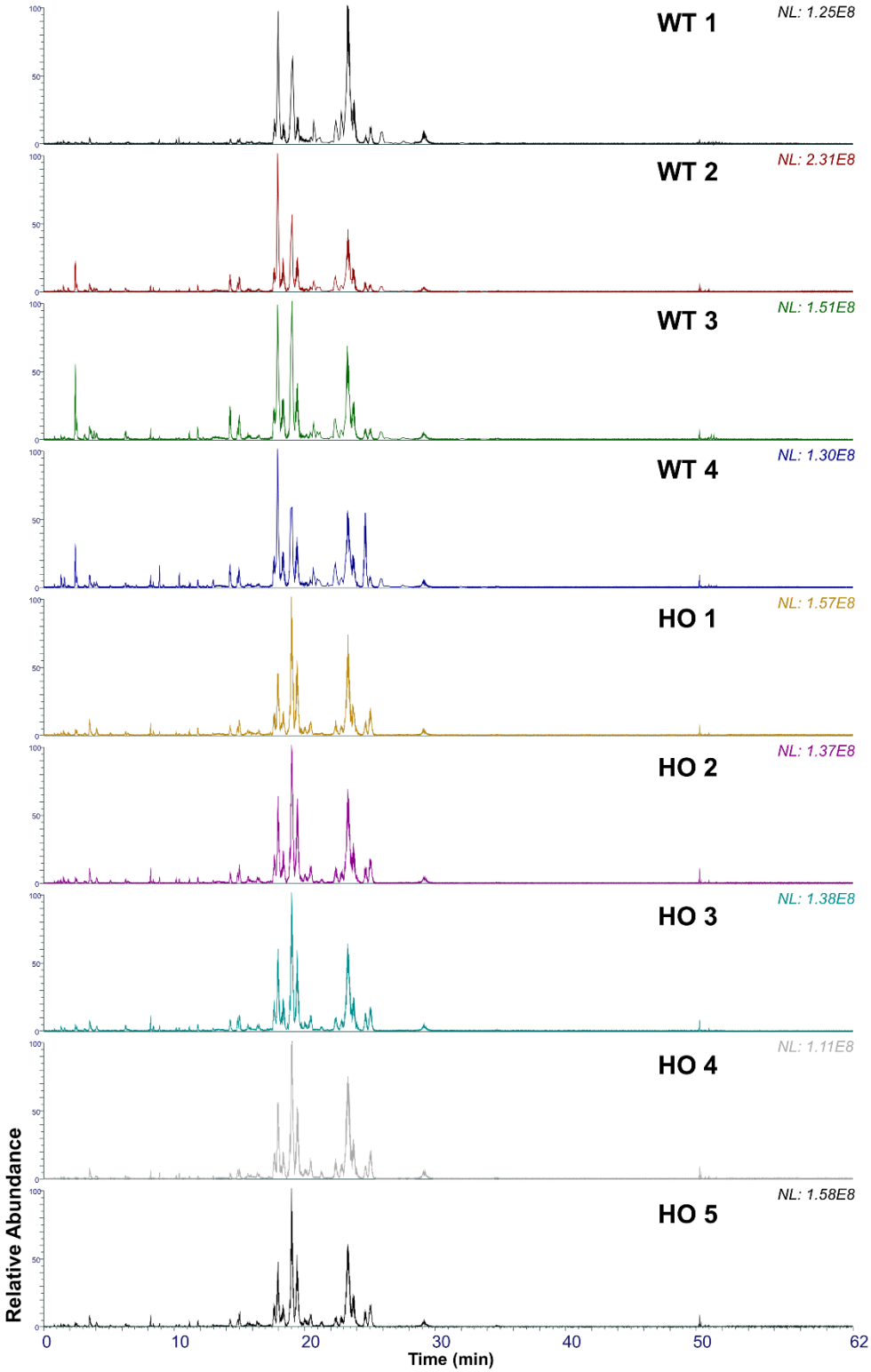

Figure S13. Adducts, lipid classes, and fragmentation rules for generation of a custom LipiDex library for automated identification of plasmenyl and plasmanyl PE and PC lipids from negative-mode HCD-MS data.

Adducts

Name	Formula	Loss	Polarity	Charge
[M-H]-	H-1	true	-	1
[M+FA-H]-	H1C1O2	true	-	1

Lipid Classes

Name	Abbreviation	Head Group	Adducts	Backbone	Num. Fatty Acids	Optimal Polarity	sn1	sn2	sn3	sn4
Plasmanyl Phosphatidylethanolamine	Plasmanyl-PE	C2H7N1O4P1	[M-H]-	Glycerol	2	-	Ether	Alkyl	-	-
Phosphatidylcholine	PC	C5H13N1O4P1	[M+FA-H]-	Glycerol	2	-	Alkyl	Alkyl	-	-
Phosphatidylethanolamine	PE	C2H7N1O4P1	[M-H]-	Glycerol	2	-	Alkyl	Alkyl	-	-
Plasmenylphosphatidylcholine	Plasmenyl-PC	C5H13N1O4P1	[M+FA-H]-	Glycerol	2	-	Plasmenyl	Alkyl	-	-
Plasmenylphosphatidylethanolamine	Plasmenyl-PE	C2H7N1O4P1	[M-H]-	Glycerol	2	-	Plasmenyl	Alkyl	-	-
Plasmanyl Phosphatidycholine	Plasmanyl-PC	C5H13N1O4P1	[M+FA-H]-	Glycerol	2	-	Ether	Alkyl	-	-

Fragmentation Rules

```
Fragmentation Library
PC [M+FA-H]-
    C7H15O5N1P1          50   1  Fragment
    C4H11O4N1P1          50   1  Fragment
    -                    50   1  Alkyl Fragment
    C-2H-4O-2            100  1  Neutral Loss
PE [M-H]-
    C-1O-2               200  1  PUFA Fragment
    -                    999  1  Alkyl Fragment
    P1O3                 50   1  Fragment
    C2H7O4N1P1           50   1  Fragment
    C5H11O5N1P1          50   1  Fragment
Plasmanyl-PC [M+FA-H]-
    -                    999  1  Alkyl Fragment
    C-2H-4O-2            100  1  Neutral Loss
Plasmanyl-PE [M-H]-
    P1O3                 100  1  Fragment
    C2H7O4N1P1           100  1  Fragment
    C-5H-6O-2            50   1  PUFA Fragment
    C-1O-2               150  1  PUFA Fragment
    -                    999  1  Alkyl Fragment
    H-1                  50   1  Alkyl Neutral Loss
    H1O1                 200  1  Alkyl Neutral Loss
Plasmenyl-PC [M+FA-H]-
    -                    999  1  Alkyl Fragment
    C-2H-4O-2            100  1  Neutral Loss
Plasmenyl-PE [M-H]-
    P1O3                 250  1  Fragment
    C2H7O4N1P1           250  1  Fragment
    C5H11O5N1P1          200  1  Fragment
    C-5H-6O-2            250  1  PUFA Fragment
    C-1O-2               750  1  PUFA Fragment
    -                    999  1  Alkyl Fragment
    H1O1                 50   1  Alkyl Neutral Loss
```

Figure S14: Bar graphs of the fold change in the relative abundance of non-ether PEs and PCs identified in all three tissue types (cerebellum, hippocampus, cortex) containing either 20:4 or 22:6 acyl chains.

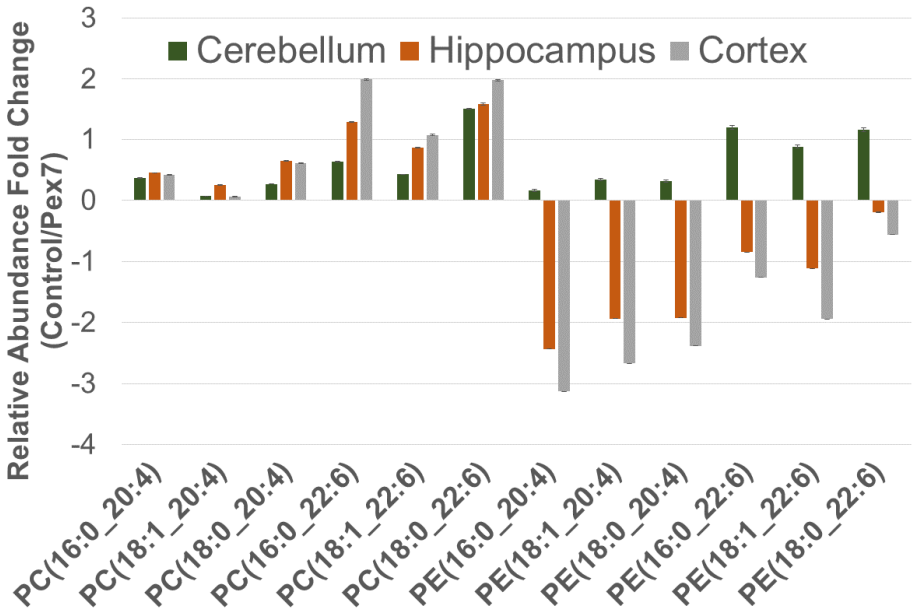

Table S1. Structures of PE and PC ether lipid standards with corresponding positive and negative mode precursor ion *m/z* values along with observed ppm error values.

Name	Structure	m/z_{obs} $[M+H]^+$	m/z_{theo} $[M+H]^+$	ppm error	m/z_{obs} $[M-H]^-$ or $[M-H+FA]^-$	m/z_{theo} $[M-H]^-$ or $[M-H+FA]^-$	ppm error
PE(*O*-16:0/18:1(9*Z*))	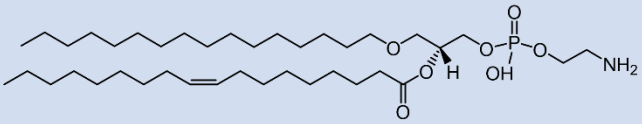	704.5592	704.5589	0.4	702.5472	702.5443	4.1
PE(*P*-18:0/18:1(9*Z*))	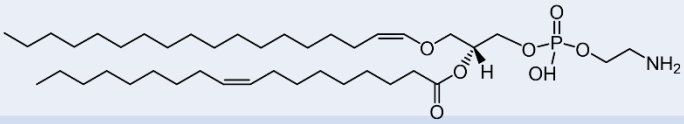	730.5759	730.5745	1.9	728.5689	728.5600	12.2
PC(*O*-16:0/18:1(9*Z*))	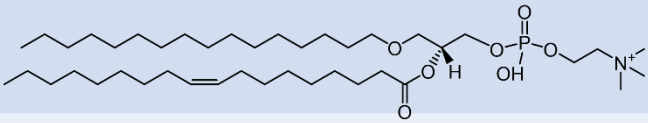	772.6222	772.6215	0.9	790.5986	790.5967	2.4
PC(*P*-18:0/18:1(9*Z*))	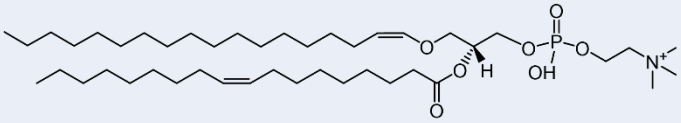	746.6071	746.6058	1.7	816.6157	816.6124	4.0

Table S2. Tabulation of fragment ion assignments with ppm error values for positive-mode HCD fragmentation of singly protonated PE and PC ether lipid standards.

m/z_{obs}	m/z_{theo}	error (ppm)
PE(*O*-16:0/18:1(9*Z*))		
661.5167	661.5172	-0.8
563.5373	563.5403	-5.3
462.2971	462.2927	9.5
440.313	440.3136	-1.4
265.2521	265.2531	-3.8
PE(*P*-18:0/18:1(9*Z*))		
589.554	589.556	-3.4
466.3284	466.3292	-1.7
462.2956	462.2979	-5.0
448.3186	448.3174	2.7
392.2913	392.2924	-2.8
339.2878	339.2894	-4.7
265.2519	265.2531	-4.5
PC(*P*-18:0/18:1(9*Z*))		
589.5543	589.556	-2.9
504.3439	504.3449	-2.0
508.3752	508.3762	-2.0
490.3645	490.3656	-2.2
265.2523	265.2531	-3.0
184.0733	184.0725	4.3
PC(*O*-16:0/18:1(9*Z*))		
563.5387	563.5403	-2.8
504.344	504.3449	-1.8
482.3594	482.3605	-2.3
464.3488	464.3499	-2.4
265.2534	265.2531	1.1
184.0725	184.0725	0.0

Table S3. Tabulation of fragment ion assignments with ppm error values for negative-mode HCD fragmentation of deprotonated ether lipid standards.

m/z_{obs}	m/z_{theo}	error (ppm)
PE(*O*-16:0/18:1(9*Z*))		
659.5011	659.5021	-1.5
420.2875	420.2884	-2.1
438.298	438.299	-2.3
281.2469	281.2481	-4.3
PE(*P*-18:0/18:1(9*Z*))		
464.3142	464.3147	-1.1
460.2834	460.2834	0.0
446.3038	446.3041	-0.7
281.2474	281.2486	-4.3
152.9962	152.9958	2.6
267.2688	267.2691	-1.1
PC(*P*-18:0/18:1(9*Z*))		
756.5893	756.5913	-2.6
711.5311	711.5334	-3.2
685.5163	685.5178	-2.2
488.3138	488.3146	-1.6
492.3447	492.346	-2.6
474.3346	474.3354	-1.7
281.2471	281.2486	-5.3
267.2686	267.2691	-1.9
168.0431	168.0431	0.0
PC(*O*-16:0/18:1(9*Z*))		
730.5740	730.5756	-2.2
685.5163	685.5178	-2.2
659.5005	659.5021	-2.4
466.3292	466.3303	-2.4
448.3189	448.3197	-1.8
281.2470	281.2486	-5.7
168.0426	168.0431	-3.0

Table S4. Tabulation of fragment ion assignments with ppm error values for positive-mode 213 nm UVPD fragmentation of singly protonated PE and PC ether lipid standards.

m/z_{obs}	m/z_{theo}	error (ppm)
PE(*O*-16:0/18:1(9*Z*)), 50 ms		
563.5389	563.5403	-2.5
440.3144	440.3136	1.8
576.4026	576.4024	0.3
590.4167	590.4180	-2.2
PE(*P*-18:0/18:1(9*Z*)), 50 ms		
462.2985	462.2979	1.3
463.3053	463.3057	-0.9
464.3147	464.3136	2.4
589.5551	589.5560	-1.5
602.4078	602.4180	-16.9
616.4279	616.4337	-9.4
466.3275	466.3292	-3.6
339.2891	339.2894	-0.9
263.2375	263.2375	0.0
392.2920	392.2924	-1.0
PC(*P*-18:0/18:1(9*Z*)), 600 ms		
504.3446	504.3449	-0.6
505.3527	505.3527	0.0
506.3606	506.3605	0.2
550.3868	550.3867	0.2
634.4826	634.4806	3.2
658.4804	658.4806	-0.3
756.5915	756.5902	1.7
508.3759	508.3762	-0.6
490.3656	490.3656	0.0
490.3273	490.3292	-3.9
262.2291	262.2297	-2.3
PC(*O*-16:0/18:1(9*Z*)), 600 ms		
524.3706	524.3711	-1.0
608.4763	608.4650	18.6
632.4677	632.4650	4.3
730.5728	730.5745	-2.3
687.5350	687.5329	3.1
482.3606	482.3605	0.2
480.3423	480.3449	-5.4
464.3500	464.3499	0.2
465.3569	465.3578	-1.9

Table S5. Tabulation of fragment ion assignments with ppm error values for negative-mode 213 nm UVPD fragmentation of deprotonated PE and PC ether lipid standards.

m/z_{obs}	m/z_{theo}	error (ppm)
PE(*O*-16:0/18:1(9*Z*)), 50 ms		
673.5173	673.5172	0.1
672.5085	672.5094	-1.3
659.4990	659.5016	-3.9
438.2979	438.3020	-9.4
420.2864	420.2884	-4.8
418.2729	418.2717	2.9
281.2485	281.2481	1.4
PE(*P*-18:0/18:1(9*Z*)), 50 ms		
698.5231	698.5256	-3.6
699.5260	699.5334	-10.6
685.5147	685.5178	-4.5
464.3135	464.3146	-2.4
462.2973	462.2990	-3.7
460.2819	460.2833	-3.0
461.2892	461.2912	-4.3
281.2472	281.2481	-3.2
267.2667	267.2688	-7.9
PC(*P*-18:0/18:1(9*Z*)), 600ms		
756.5863	756.5913	-6.6
685.5141	685.5178	-5.4
488.3118	488.3146	-5.7
492.3432	492.346	-5.7
474.3328	474.3354	-5.5
281.2467	281.2486	-6.8
267.2678	267.2691	-4.9
712.5412	712.5378	4.8
711.5297	711.5334	-5.2
474.2978	474.299	-2.5
506.3224	506.3252	-5.5
490.3275	490.3303	-5.7
489.3197	489.3225	-5.7
PC(*O*-16:0/18:1(9*Z*)), 600ms		
730.5714	730.5756	-5.7
686.5221	686.5256	-5.1
685.5145	685.5178	-4.8
673.5143	673.5178	-5.2
659.4988	659.5021	-5.0
466.3278	466.3303	-5.4
448.3178	448.3197	-4.2
281.2469	281.2486	-6.0

Table S6. Structures of PE and PC lipid standards used for LC-MS separation evaluation.

Name	Structure	m/z_{obs} $[M+H]^+$	m/z_{theo} $[M+H]^+$	Error m/z $[M+H]^+$ (ppm)
PE(16:0/18:1(9Z))	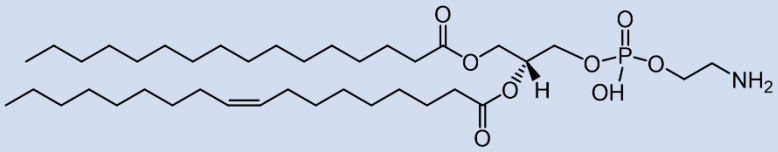	718.5385	718.5381	0.56
PC(18:0/18:1(9Z))	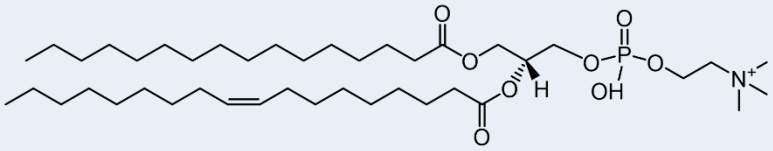	788.6159	788.6164	-0.63

Table S7. Structures of PE and PC lipid standards used as internal standards.

Name	Structure	m/z_{obs} $[M+H]^+$	m/z_{theo} $[M+H]^+$	Error m/z $[M+H]^+$ (ppm)
PE(*P*-18:0/18:1-d_9(9Z))	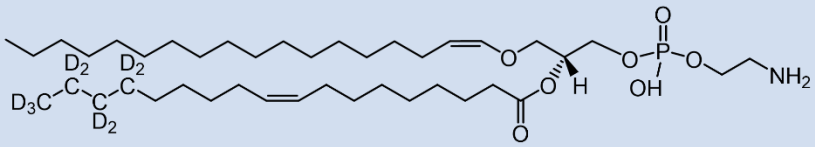	739.6338	739.6310	3.78
PC(*P*-16:0/16:0-d_9)	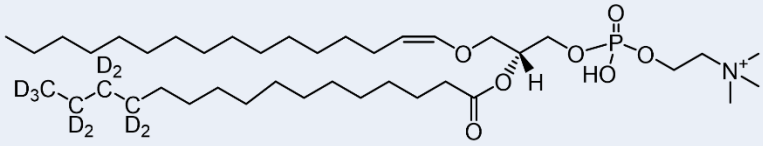	727.6340	727.6310	4.12
PC(*P*-18:0/18:1-d_9(9Z))	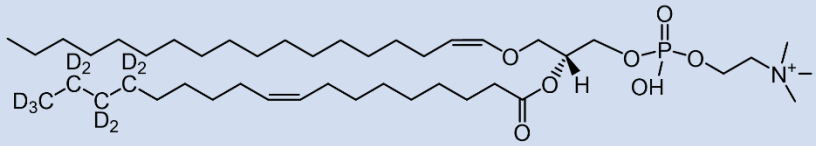	781.6771	781.6780	-1.15

Table S8. Tabulation of mouse tissue samples used for this study along with sample codes. WT, HT, and HO genotypes represent Pex7$^{WT/WT}$, Pex7$^{WT/null}$, and Pex7$^{null/null}$ mice, for **(a)** hippocampus and cerebellum samples, and **(b)** cortex samples.

(a) Tissue type	**Genotype**								
	WT 1	**WT 2**	**WT 3**	**WT 4**	**HT 1**	**HT 2**	**HO 1**	**HO 2**	**HO 3**
Cerebellum	C1	C2	C3	C4	C5	C6	C7	C8	C9
Hippocampus	H1	H2	H3	H4	H5	H6	H7	H8	H9

(b) Tissue type	**Genotype**								
	WT 1	**WT 2**	**WT 3**	**WT 4**	**HO 1**	**HO 2**	**HO 3**	**HO 4**	**HO 5**
Cortex	X1	X2	X3	X4	X5	X6	X7	X8	X9

Table S9. Tabulation of precursor and fragment ion assignments with ppm error values for negative-mode HCD fragmentation of singly deprotonated ether lipids identified across all mouse tissue extracts, along with protonated precursor *m/z* values and retention time ranges used for targeted LC/UVPD-MS runs.

Lipid ID	Precursor *m/z* ([M-H]$^-$)			*sn*-2 acyl chain product ion			*sn*-1 vinyl ether chain product ion			*sn*-1 vinyl ether chain neutral loss ion			Theoretical [M+H]$^+$ *m/z*
	Experimental	Theoretical	ppm error	Experimental	Theoretical	ppm error	Experimental	Theoretical	ppm error	Experimental	Theoretical	ppm error	
PE(*P*-16:0/22:6)	746.5097	746.5130	-4.4	327.2299	327.2330	-9.5	239.2359	239.2380	-8.8	506.2652	506.2677	-4.9	748.5276
PE(*P*-18:2/20:4)	746.5157		3.6	303.2333	303.2330	1.0	263.2367	263.2380	-4.9	-	482.2677	-	
PE(*P*-18:1/22:6)	772.5259	772.5287	-3.6	327.2302	327.2330	-8.6	265.2513	265.2537	-9.0	506.2638	506.2677	-7.7	774.5423
PE(*P*-16:0/20:4)	722.5093	722.5130	-5.1	303.2303	303.2330	-8.9	239.2357	239.2380	-9.6	482.2649	482.2677	-5.8	724.5276
PE(*P*-18:1/20:4)	748.5253	748.5287	-4.5	303.2302	303.2330	-9.2	265.2514	265.2537	-8.7	482.2647	482.2677	-6.2	750.5432
PE(*P*-18:0/22:6)	774.5426	774.5443	-2.2	327.2303	327.2330	-8.3	267.2669	267.2693	-9.0	506.2639	506.2677	-7.5	776.5589
PE(*P*-16:0/18:1)	700.5232	700.5287	-7.9	281.2461	281.2486	-8.9	239.2356	239.2380	-10.0	460.2794	460.2833	-8.5	702.5432
PE(*P*-18:1/16:0)				255.2306	255.2330	-9.4	265.2512	265.2537	-9.4	-	434.2677	-	
PE(*P*-18:1/18:1)	726.5416	726.5443	-3.7	281.2462	281.2486	-8.5	265.2513	265.2537	-9.0	460.2805	460.2833	-6.1	728.5589
PE(*P*-18:0/20:4)	750.5388	750.5443	-7.3	303.2304	303.2330	-8.6	267.2671	267.2693	-8.2	482.2624	482.2677	-11.0	752.5589
PE(*P*-16:0/22:4)	750.5452		1.2	331.2647	331.2643	1.2	239.2383	239.2380	1.3	510.3000	510.2990	-2.0	
PE(*P*-18:0/22:4)	778.5696	778.5756	-7.7	331.2614	331.2643	-8.8	267.2670	267.2693	-8.6	510.2986	510.2990	-0.8	780.5902
PE(*P*-18:0/18:1)	728.5547	728.5600	-7.3	281.2461	281.2486	-8.9	267.2669	267.2693	-9.0	460.2796	460.2833	-8.0	730.5745
PE(*P*-16:0/20:1)	728.5606		0.8	309.2804	309.2799	1.6	239.2384	239.2380	1.7	-	488.3146	-	
PE(*P*-18:1/20:1)	754.5696	754.5756	-8.0	309.2767	309.2799	-10.3	265.2511	265.2537	-9.8	488.3103	488.3146	-8.8	756.5902
PE(*P*-18:2/22:6)	770.5160	770.5130	3.9	327.2332	327.2330	0.6	263.2380	263.2380	0.0	506.2701	506.2677	4.7	772.5276
PE(*P*-18:1/22:4)	776.5610	776.5600	1.3	331.2645	331.2643	0.6	-	265.2537	-	-	510.2990	-	778.5746

Table S10: Summary of the four most abundant ether lipids across all tissue types (cerebellum, hippocampus, cortex) with corresponding C=C double bond location fragment ion assignments and accompanying ppm error values.

Lipid ID	m/z_{Theo}	m/z_{exp}	ppm error	Double bond Position
PE(*P*-16:0_22:6)	692.4650	692.4616	-4.9	Δ19
	680.4650	680.4667	2.5	Δ16
	652.4337	652.4335	-0.3	
	640.4337	640.4323	-2.2	Δ13
	612.4024	612.4024	0.0	
	600.4024	600.4022	-0.3	Δ10
	572.3711	572.3716	0.9	
	560.3711	560.3702	-1.6	Δ7
	532.3398	532.3386	-2.3	
	520.3398	520.3390	-1.5	Δ4
PE(*P*-18:0_22:6)	720.4963	720.4964	0.1	Δ19
	708.4963	708.4965	0.3	Δ16
	680.4650	680.4652	0.3	
	668.4650	668.4643	-1.0	Δ13
	640.4337	640.4333	-0.6	
	628.4337	628.4346	1.4	Δ10
	600.4024	600.4022	-0.3	
	588.4024	588.4043	3.2	Δ7
	560.3711	560.3700	-2.0	
	548.3711	548.3702	-1.6	Δ4
PE(*P*-18:1_22:6)	718.4806	718.4817	1.5	Δ19
	706.4806	706.4828	3.1	Δ16
	678.4493	678.4510	2.5	
	666.4499	666.4500	0.2	Δ13
	638.4180	638.4188	1.3	
	626.4186	626.4213	4.3	Δ10
	598.3867	598.3881	2.3	
	586.3873	586.3843	-5.1	Δ7
	558.3554	558.3567	2.3	
PE(*P*-18:1_20:4)	652.4337	652.4332	-0.8	Δ14
	640.4337	640.4331	-0.9	Δ11
	612.4024	612.4024	0.0	
	600.4024	600.4027	0.5	Δ8
	572.3711	572.3707	-0.7	

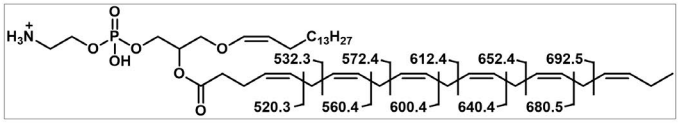

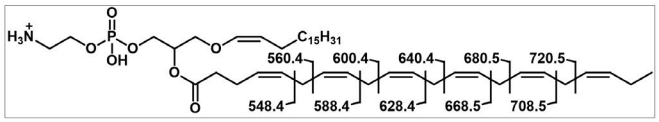

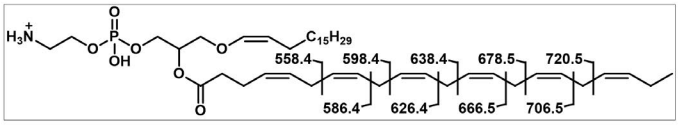

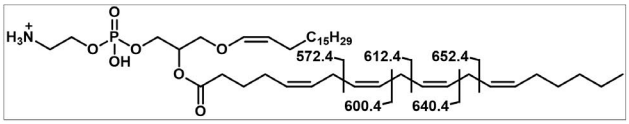

Background

Glycerophospholipids are the main component of cell membranes and are highly diverse in both their structure and size.[1] These lipids are composed of two hydrophobic fatty acid chains linked to a hydrophilic headgroup via a connecting glycerol backbone. GP headgroups include phosphatidylcholine (PC), phosphatidylglycerol (PG), phosphatidic acid (PA), phosphatidylserine (PS), phosphatidylinositol (PI), and phosphatidylethanolamine (PE). In addition to headgroup variation, GPs can vary in their fatty acid chain lengths (i.e., number of carbon atoms), *sn*-stereochemistry, and their degree, type, location, and stereochemistry of unsaturation elements. Additionally, while GPs with two ester-linked fatty acids are most common, GPs can also vary in their linkage type, i.e. ester, ether (plasmanyl), or vinyl ether (plasmenyl/plasmalogen). Plasmalogens comprise about 18% of phospholipids in mammalian cells[2], and are especially abundant in the inner leaflet of plasma membranes.[3] Plasmalogens alter physiochemical cellular properties, packing density, and conformational order of GPs within cellular membranes, thus conferring a profound effect on membrane fluidity, thickness, and lateral pressure.[4–7] Specifically, conversion of the ester to ether or vinyl ether bond at the *sn*-1 position allows tighter packing of membrane lipids, thus reducing membrane fluidity.[8] Plasmalogens also function as cellular antioxidants,[9] and are considered to be important sources of omega-3 fatty acid docosahexaenoic acid (DHA), and omega-6 fatty acid, arachidonic acid (AA), both of which play crucial roles in development of brain and retina.[10] Furthermore, plasmalogens confer anti-inflammatory properties[11], are implicated in ferroptosis,[12,13] and are especially crucial during development.[8] Specific ether lipids have also been identified as markers for endothelial cell differentiation[31] and various cancers.[15,16] It is important to note that only certain GP classes exist in plasmenyl or plasmanyl form,[17] namely primarily as PEs or PCs in mammalian systems, although some rare ether-linked PS, PA, PI and PT GPs have been discovered.[18] Within the PE and PC ether lipid subtypes, PEs primarily exist as plasmalogens, containing a vinyl ether linkage (i.e., PE-*P*), while PCs exist primarily as plasmanyl lipids, containing an ether linkage (i.e., PC-*O*).[19,20]

The initial, committing steps in ether phospholipid synthesis occur in peroxisomes and result in the biosynthesis of alkylglycerol. This involves dehydrogenation of glycerol-3-phosphate (G3P) via enzyme glyceraldehyde-3-phosphate dehydrogenase (G3PDH) to form dihydroxyacetone phosphate (DHAP), which is subsequently acylated by Acyl-CoA to form acyl-DHAP.[21] Acyl-DHAP can then be converted to alkyl-DHAP by the alkyl DHAP synthase enzyme (ADHAPS). Finally, the alkyl DHAP is reduced to 1-*O*-alkyl G3P (AGP) by alkyl DHAP reductase (ADHAPR). The remaining steps to generate a mature ether phospholipid occur in the endoplasmic reticulum (ER) and involve the addition of the polar head group, a fatty acid at the *sn*-2 position, and a vinyl ether bond at the *sn*-1 position. The main two pathways in the ER include conversion of AGP to alkyl-acylglycerol (AAG), as well as addition of a cytidine

diphosphate-alcohol group at the sn-3 position to form the final mature ether phospholipid.[22] Plasmalogen levels are thought to be regulated by feedback inhibition through FAR1, located on the peroxisome membrane. While synthesis of traditional di-acyl GPs is well-characterized in the literature, much of the literature relating to ether GPs after the peroxisomal steps is lacking, with notable recent advances including identification of the human desaturase enzyme responsible for conversion of the PE-*O* alkyl ether linkage to a PE-*P* vinyl ether linkage in 2019,[23] while the gene that encodes this enzyme was just discovered in 2020.[24] Ethanolamine phosphotransferase (EPT1) is required to produce ethanolamine phospholipids, and deficiency of this enzyme causes marked decrease in plasmenyl-PE species.[25]

(1) Hishikawa, D.; Hashidate, T.; Shimizu, T.; Shindou, H. Diversity and Function of Membrane Glycerophospholipids Generated by the Remodeling Pathway in Mammalian Cells. *J. Lipid. Res.* **2014**, *55*, 799–807.
(2) Wallner, S.; Orsó, E.; Grandl, M.; Konovalova, T.; Liebisch, G.; Schmitz, G. Phosphatidylcholine and Phosphatidylethanolamine Plasmalogens in Lipid Loaded Human Macrophages. *PLoS One* **2018**, *13*, e0205706.
(3) Lorent, J. H.; Levental, K. R.; Ganesan, L.; Rivera-Longsworth, G.; Sezgin, E.; Doktorova, M.; Lyman, E.; Levental, I. Plasma Membranes Are Asymmetric in Lipid Unsaturation, Packing and Protein Shape. *Na.t Chem. Biol.* **2020**, *16*, 644–652.
(4) Almsherqi, Z. A. Potential Role of Plasmalogens in the Modulation of Biomembrane Morphology. *Front. Cell Dev. Biol.* **2021**, *9*, 1648.
(5) Nagan, N.; Zoeller, R. A. Plasmalogens: Biosynthesis and Functions. *Prog. Lipid Res.* **2001**, *40*, 199–229.
(6) Dean, J. M.; Lodhi, I. J. Structural and Functional Roles of Ether Lipids. *Protein Cell* **2018**, *9*, 196–206.
(7) Koivuniemi, A. The Biophysical Properties of Plasmalogens Originating from Their Unique Molecular Architecture. *FEBS Lett.* **2017**, *591*, 2700–2713.
(8) Drechsler, R.; Chen, S.-W.; Dancy, B. C. R.; Mehrabkhani, L.; Olsen, C. P. HPLC-Based Mass Spectrometry Characterizes the Phospholipid Alterations in Ether-Linked Lipid Deficiency Models Following Oxidative Stress. *PLoS One* **2016**, *11*, e0167229.
(9) Paltauf, F. Ether Lipids in Biomembranes. *Chem. Phys. Lipids* **1994**, *74*, 101-139.
(10) Hishikawa, D.; Valentine, W. J.; Iizuka-Hishikawa, Y.; Shindou, H.; Shimizu, T. Metabolism and Functions of Docosahexaenoic Acid-Containing Membrane Glycerophospholipids. *FEBS Lett.* **2017**, *591*, 2730–2744.
(11) Nguma, E.; Yamashita, S.; Kumagai, K.; Otoki, Y.; Yamamoto, A.; Eitsuka, T.; Nakagawa, K.; Miyazawa, T.; Kinoshita, M. Ethanolamine Plasmalogen Suppresses Apoptosis in Human Intestinal Tract Cells in Vitro by Attenuating Induced Inflammatory Stress. *ACS Omega* **2021**, *6*, 3140–3148.
(12) Zou, Y.; Henry, W. S.; Ricq, E. L.; Graham, E. T.; Phadnis, V. V.; Maretich, P.; Paradkar, S.; Boehnke, N.; Deik, A. A.; Reinhardt, F.; Eaton, J. K.; Ferguson, B.; Wang, W.; Fairman, J.; Keys, H. R.; Dančík, V.; Clish, C. B.; Clemons, P. A.; Hammond, P. T.; Boyer, L. A.; Weinberg, R. A.; Schreiber, S. L. Plasticity of Ether Lipids Promotes Ferroptosis Susceptibility and Evasion. *Nature* **2020**, *585*, 603–608.
(13) Cui, W.; Liu, D.; Gu, W.; Chu, B. Peroxisome-Driven Ether-Linked Phospholipids Biosynthesis Is Essential for Ferroptosis. *Cell Death Differ.* **2021**, *28*, 2536–2551.
(14) Nakamura, Y.; Shimizu, Y.; Horibata, Y.; Tei, R.; Koike, R.; Masawa, M.; Watanabe, T.; Shiobara, T.; Arai, R.; Chibana, K.; Takemasa, A.; Sugimoto, H.; Ishii, Y. Changes of

Plasmalogen Phospholipid Levels during Differentiation of Induced Pluripotent Stem Cells 409B2 to Endothelial Phenotype Cells. *Sci. Rep.* **2017**, *7*, 9377.
(15) Fernandes, A. M. A. P.; Messias, M. C. F.; Duarte, G. H. B.; de Santis, G. K. D.; Mecatti, G. C.; Porcari, A. M.; Murgu, M.; Simionato, A. V. C.; Rocha, T.; Martinez, C. A. R.; Carvalho, P. O. Plasma Lipid Profile Reveals Plasmalogens as Potential Biomarkers for Colon Cancer Screening. *Metabolites* **2020**, *10*, 262.
(16) Messias, M. C. F.; Mecatti, G. C.; Priolli, D. G.; de Oliveira Carvalho, P. Plasmalogen Lipids: Functional Mechanism and Their Involvement in Gastrointestinal Cancer. *Lipids Health Dis.* **2018**, *17*, 41.
(17) Milne, S.; Ivanova, P.; Forrester, J.; Alex Brown, H. Lipidomics: An Analysis of Cellular Lipids by ESI-MS. *Methods* **2006**, *39*, 92–103.
(18) Ivanova, P. T.; Milne, S. B.; Brown, H. A. Identification of Atypical Ether-Linked Glycerophospholipid Species in Macrophages by Mass Spectrometry. *J. Lipid Res.* **2010**, *51*, 1581–1590.
(19) Mawatari, S.; Sasuga, Y.; Morisaki, T.; Okubo, M.; Emura, T.; Fujino, T. Identification of Plasmalogens in Bifidobacterium Longum, but Not in Bifidobacterium Animalis. *Sci. Rep.* **2020**, *10*, 427.
(20) Imbs, A. B.; Dang, L. P. T.; Nguyen, K. B. Comparative Lipidomic Analysis of Phospholipids of Hydrocorals and Corals from Tropical and Cold-Water Regions. *PLOS ONE* **2019**, *14*, e0215759.
(21) Lodhi, I. J.; Semenkovich, C. F. Peroxisomes: A Nexus for Lipid Metabolism and Cellular Signaling. *Cell Metab.* **2014**, *19*, 380–392.
(22) Dean, J. M.; Lodhi, I. J. Structural and Functional Roles of Ether Lipids. Protein Cell 2018, 9, 196–206.
(23) Gallego-García, A.; Monera-Girona, A. J.; Pajares-Martínez, E.; Bastida-Martínez, E.; Pérez-Castaño, R.; Iniesta, A. A.; Fontes, M.; Padmanabhan, S.; Elías-Arnanz, M. A Bacterial Light Response Reveals an Orphan Desaturase for Human Plasmalogen Synthesis. *Science* **2019**, *366*, 128–132.
(24) Werner, E. R.; Keller, M. A.; Sailer, S.; Lackner, K.; Koch, J.; Hermann, M.; Coassin, S.; Golderer, G.; Werner-Felmayer, G.; Zoeller, R. A.; Hulo, N.; Berger, J.; Watschinger, K. The TMEM189 Gene Encodes Plasmanylethanolamine Desaturase Which Introduces the Characteristic Vinyl Ether Double Bond into Plasmalogens. *Proc. Natl. Acad. Sci. U. S. A.* **2020**, *117*, 7792–7798.
(25) Horibata, Y.; Elpeleg, O.; Eran, A.; Hirabayashi, Y.; Savitzki, D.; Tal, G.; Mandel, H.; Sugimoto, H. EPT1 (Selenoprotein I) Is Critical for the Neural Development and Maintenance of Plasmalogen in Humans. *J. Lipid Res.* **2018**, *59*, 1015–1026.

Experimental details

Materials

LC-MS grade OmniSolv methanol, acetonitrile, and water were purchased from VWR. LC-MS grade chloroform was purchased from Sigma Aldrich. LC-MS grade isopropanol, ammonium formate, and formic acid were purchased from Fisher Scientific. Pure lipid standards PC(*P*-18:0/18:1(9*Z*)), PC(*O*-16:0/18:1(9*Z*)), PE(*P*-18:0/18:1(9*Z*)), PE(*O*-16:0/18:1(9*Z*)), PE(*P*-18:0/18:1-d_9(9*Z*)), PE(16:0/18:1(9*Z*)), and PC(18:0/18:1(9*Z*)) were purchased from Avanti Polar Lipids. PC(*P*-16:0/16:0-d_9) was purchased from Cayman Chemical Company.

Murine samples

The mice used were B6;129S6-Pex7$^{tm2.3Brav}$, also referred as Pex7$^{null/null}$, derived from the Pex7 hypomorphic mouse model (B6;129S6-Pex7$^{tm2.0Brav}$) as described previously.[1] Pex7$^{null/null}$ mice were generated by breeding Pex7$^{WT/null}$ heterozygotes. Around 20% of Pex7$^{null/null}$ mice survive weaning. PCR primer pairs for genotyping the wild type and null alleles were respectively: (forward primer 5′- GGC ACA CTT CCA GCA ATA- 3′; reverse primer 5′-GGT GGG GTG GGA TTA GAT AAA- 3′) and (forward primer 5′- GGG GCA AGT CTT TTG AAG TC- 3′; reverse primer 5′- GAG CAG GTA GTG GCT TTC TA). *Mice were housed in the animal care facility of* the Research Institute of McGill University Health Centre and fed *ad libitum* with rodent diet (18% protein) from Teklad Global, Envigo and free water access. Three month old Pex7$^{null/null}$ mice and their control littermates (Pex7$^{WT/null}$ and Pex7$^{WT/WT}$) were anesthetized with 5% isoflurane and euthanized by CO_2 exposure after loss of consciousness. Similar numbers of males and females were sacrificed with no differences detected. Blood was collected by cardiac puncture, followed by perfusion with PBS and tissues were collected. Cerebral cortex, cerebellum, and hippocampus were collected and snap frozen in liquid nitrogen and stored at 80°C until lipid extractions were performed.

Tissue homogenization and lipid extractions

For each extraction, ~30 mg (16-44 mg) of frozen tissue (9 hippocampus samples, 9 cerebellum samples) was transferred to a bead mill tube pre-filled with 2.8 mm ceramic beads (Fisher Scientific) and 600 µL of methanol and 50 µL of each of the two 100 µM deuterated lipid internal standards, PE(*P*-18:0/18:1-d_9(9*Z*)) and PC(*P*-16:0/16:0-d_9) or PC(*P*-18:0/18:1-d_9(9*Z*)). The tubes were placed in a Bead Mill 4 Homogenizer (Fisher Scientific) and homogenized at level 5 for 120 seconds. Samples were then centrifuged for 1 minute at 1,000 rcf, and 500 µL of tissue homogenate was removed off the top and transferred to a 2 mL glass vial for lipid extraction. Lipid extractions were performed using a modified Bligh Dyer procedure.[2] 250 µL of water and 375 µL of chloroform were added to the 500 µL of tissue homogenate

to give a final solvent ratio of 1:1.5:2 (water:chloroform:methanol). Samples were vortexed for 30 seconds prior to filtration. Chloroform-compatible PVDF syringe filters (0.22 µm, 4 mm, Tisch Scientific) were connected to a 2.5 mL Hamilton Luer-Lok syringe (Fisher Scientific) and pre-wet with methanol prior to filtering using Luer-Lok-compatible blunt fill needles (BD, Fisher Scientific, 18 G, 1.5 in). Filtered samples were transferred to new 2 mL glass vials and left to stand at room temperature for ~5 minutes until phase separation was apparent. The organic (bottom) layer was transferred to a 300 µL glass vial insert and evaporated to dryness using a SpeedVac vacuum concentrator (Thermo Fisher Scientific). Samples were stored in the -20 °C freezer until analysis, at which point dry lipid extracts were resuspended in 50 µL of solvent (mobile phase starting conditions).

Direct infusion experiments

All experiments were performed on an Orbitrap Fusion Lumos™ Tribrid mass spectrometer (Thermo Fisher Scientific) equipped with a solid-state 213 nm CryLaS Nd:YAG laser (1.5 uJ/pulse at a repetition rate of 2.5 kHz). Direct infusion of lipid standards were performed by diluting lipids to 10 uM in methanol for positive mode ESI, or 50:50 methanol:water with 5 mM ammonium formate for PC lipids in the negative mode. Approximately 10 uL of sample was loaded into in-house gold/palladium-coated pulled tip glass capillaries (1.2 mm outer diameter and 0.69 mm inner diameter). A Nanospray Flex ion source (Thermo Fisher Scientific) was utilized for all direct infusion experiments. The ion transfer tube temperature was set to 275 °C, and spray voltages were set to +/- 1.0 kV for all experiments. MS1 and MS^2 mass spectra were collected at a resolution of 30,000 at *m/z* 200. All lipids were singly charged and isolated using a width of 1 *m/z* using quadrupole isolation. MS^2 mass spectra were collected using an AGC target of 1e6 and averaging 5 scans total (with 3 µscans per scan). HCD was performed using normalized collisions energies (NCE) ranging from 18-30. 213 nm UVPD was performed in the low-pressure trap of the dual linear ion trap using activation periods of 50 ms (125 laser pulses) and 600 ms (1500 laser pulses) for PE and PC lipids, respectively.

Untargeted LC/HCD-MS experiments

Glycerophospholipids were separated using RPLC as previously described.[3] In brief, lipids were separated using a binary mobile phase system of 60:40 acetonitrile:water (MPA) and 90:10 isopropanol:acetonitrile (MPB), each constituted with 10 mM ammonium formate and 0.1% formic acid. Lipids were diluted to approximately 50 ng/µL in mobile phase starting conditions and separated using an Acquity UPLC CSH C18 column (pore size 130 Å, 1.7 µm particle size, 2.1 mm × 100 mm, Waters) on a Dionex Ultimate 3000 UHPLC system (Thermo Fisher Scientific) coupled to the Orbitrap mass spectrometer using a heated ESI source. Glycerophospholipids were eluted using a flow rate of 260 µL/min

with the following gradient: hold at 10% B (0-2 min), 10% to 45% B (2-6 min), 45% to 60% B (6-46 min), 60% to 95% B (46-47 min), hold at 95% B (47-53 min), 95% to 10% B (53-54 min), hold at 10% B (54-62 min). A 10 µL injection volume and a column compartment temperature of 50 °C were used.

The mass spectrometer was operated in negative ion mode for untargeted LC/HCD-MS. Source parameters included an ion transfer tube temperature of 300 °C, vaporizer temperature of 40 °C, spray voltage of 3.8 kV, sheath gas setting of 5, and an auxiliary gas setting of 10. Global settings included selection of the small molecule application mode, and a total method duration of 62 minutes. All mass spectra were collected in profile mode. MS1 settings included detection in the Orbitrap at a resolution of 30,000 at *m/z* 200, normal mass range selection, a scan range of *m/z* 350-1200, an RF lens setting of 60%, an AGC target of 1e6, a maximum injection time (MIT) setting of 200 ms, and 2 µscans/scan. MS^2 data was collected using the cycle time selection for data dependent mode, with 5 seconds between master MS1 scans. Multiple filters were applied for MS2 precursor selection, including a monoisotopic peak selection (MIPS) filter in small molecule mode, an intensity threshold of 5e5, and a dynamic exclusion filter for precursors occurring 2 times within 10 seconds, with an exclusion duration of 15 seconds. A dynamic exclusion filter was used to exclude re-occurring precursor ions and isotopes with a 10 ppm error tolerance. MS^2 experiments were performed using HCD with quadrupole isolation, an isolation width of 1 *m/z*, and an HCD collision energy of 25%. HCD fragments were detected in the Orbitrap using an auto *m/z*: normal scan range, a resolution of 30,000 at *m/z* 200, and a first mass setting of *m/z* 100. Other HCD scan settings included an AGC target of 2e5, a MIT of 200 ms, and 2 µscans/scan.

Targeted LC/UVPD-MS experiments

Targeted LC/UVPD-MS experiments were performed using identical sample and LC parameters to those described for untargeted LC/HCD-MS experiments; however, in this case the ESI source was operated in positive ion mode at a spray voltage of 3.8 kV. MS^2 scans were collected using the cycle time selection for data dependent mode, with 5 seconds between master MS1 scans. Filters applied for MS^2 precursor selection included an intensity threshold of 1e5, as well as a targeted mass filter included start/end retention times and *m/z* values of protonated lipids for those corresponding lipids identified in negative-mode LC/HCD-MS runs (with 15 ppm error tolerance for precursor *m/z* values). MS^2 experiments were performed using UVPD with quadrupole isolation, an isolation width of 1 *m/z*, and a UVPD activation time of 800 ms. UVPD fragments were detected in the Orbitrap using an auto *m/z* normal scan range and a resolution of 30,000 at *m/z* 200. Other UVPD scan settings included an AGC target of 1e6, a MIT of 500 ms, and 4 µscans/scan.

Data Analysis

For assignment of all fragment ions from direct infusion-mode and LC-mode mass spectra alike, a minimum S/N threshold of 3 along with a ppm error tolerance of 20 ppm was utilized. For generation of fragment maps, ambiguous fragment ions are excluded.

LipiDex was used for automated analysis of untargeted negative-mode HCD experiments via generation of a custom LipiDex library.[4] Parameters used for this custom library are shown in **Figure S13**. The custom library was generated based off of the LipiDex_HCD_Formic library which is included in the software download package, and includes negative-mode HCD analysis for ether lipids. The custom library included six lipid classes – plasmanyl, plasmenyl, and regular di-acyl GPs, and considering both PE and PC types. All PEs were classified as $[M-H]^-$ ions, while PCs were classified as $[M+FA-H]^-$ adducts. For comprehensiveness, alkyl, plasmanyl, and plasmenyl chains for all lipid types were expanded to include 10-26 carbon atoms with 0-6 C=C double bonds, encompassing the entire range of expected GP chains in eukaryotic systems. All fragmentation rules within the custom library are also listed in **Figure S13**. Ether linkage information for all lipids was identified via manual interpretation of the negative-mode HCD mass spectra associated with plasmenyl and plasmanyl PE and PC precursors.

Quantitative analysis of ether GPs was performed using FreeStyle (Thermo Fisher Scientific). Parameters utilized for peak area determination included a Gaussian smoothing filter (level 5), parameter-less peak detection (PPD) with manual adjustments (to ensure uniformity of peak areas down to a relative abundance of 0.05) and with the merge overlapping feature enabled. Peak areas were extracted from the base peak LC-MS1 trace from LC/UVPD-MS experiments, with 10 ppm error tolerances for precursor extracted ion chromatogram (XIC) *m/z* values. Peak areas of targeted ether lipids were normalized to the deuterated internal standards as well as to tissue mass prior to extraction and were averaged for biological replicates of the same genotype. Statistical differences in individual lipid abundances between control (HT, WT) and Pex7 deficient (HO, i.e. Pex7) samples were evaluated using a two-tailed t-test (Microsoft Excel, p value cutoff of 0.05).

(1) Fallatah, W.; Smith, T.; Cui, W.; Jayasinghe, D.; Di Pietro, E.; Ritchie, S. A.; Braverman, N. Oral Administration of a Synthetic Vinyl-Ether Plasmalogen Normalizes Open Field Activity in a Mouse Model of Rhizomelic Chondrodysplasia Punctata. *Dis. Model. Mech.* **2020**, *13*, dmm042499.

(2) Bligh, E. G.; Dyer, W. J. A Rapid Method of Total Lipid Extraction and Purification. *Can. J. Biochem. Physiol.* **1959**, *37*, 911–917.

(3) Blevins, M. S.; Klein, D. R.; Brodbelt, J. S. Localization of Cyclopropane Modifications in Bacterial Lipids via 213 Nm Ultraviolet Photodissociation Mass Spectrometry. *Anal. Chem.* **2019**, *91*, 6820–6828.

(4) Hutchins, P. D.; Russell, J. D.; Coon, J. J. LipiDex: An Integrated Software Package for High-Confidence Lipid Identification. *Cell Syst.* **2018**, *6*, 621-625.e5.

Additional results

While the primary goal with this study was to identify the structures of ether lipids which have statistically significant differences in abundances between control and disease RCDP mouse samples, as well as the extent of downregulation or upregulation, we were also interested in evaluating differences in the abundances of specific diacyl (non-ether) PE and PC glycerophospholipids between the control and disease samples. This aspect of the investigation was inspired by a 2015 study in which the overall level of PE lipids in RCDP fibroblasts was tightly regulated, thus resulting in the upregulation of diacyl PEs in disease RCDP fibroblast samples (relative to the control samples).[1] Interestingly, in this same study, no changes were observed in diacyl PC levels, and diacyl PE levels were primarily elevated for PEs which contained a 20:4 acyl chain (and not for those containing 22:6 acyl chains).[1] In our present dataset, we identified a total of 12 diacyl PE or PC lipids which contained either a 20:4 or 22:6 acyl chain, including PE and PC (16:0_20:4), (18:1_20:4), (18:0_20:4), (16:0_22:6), (18:1_22:6), and (18:0_22:6). Quantitation of these lipids was undertaken as previously described for the ether lipids in this study, including normalization to both the appropriate internal standard as well as to the mass of the tissue used. The resulting data is visualized in bar graph format in **Figure S14**, in which the relative fold change in abundance (Pex7 controls/Pex7 mutants) is plotted as a function of lipid identification. Here, values above 0 indicate that a specific lipid is more abundant in the control samples, whereas values below 0 indicate that a specific lipid is more abundant in the Pex7 deficient samples. Most striking in this dataset is the distinct upregulation of all diacyl PEs (both 20:4- and 22:6) in the Pex7 deficient cerebral cortex and hippocampus samples, but not in the cerebellum (**Figure S14**).

We observe a slightly more dramatic increase in diacyl PEs which contain a 20:4 acyl chain for the Pex7 cerebral cortex and hippocampus samples. In contrast, the cerebellum PE data shows a decrease in diacyl PEs in the mutant samples, with enhanced downregulation for the 22:6 PEs in comparison to the 20:4 PEs. The six identified diacyl PCs were more abundant in the control samples for all tissue types in comparison to the Pex7 samples, especially so for the 22:6 diacyl PCs. Finally, we observe a marked increase of all diacyl PC species in the control samples compared to the Pex7 disease samples, despite a lack of PC ether lipids in any of the samples. These findings indicate that a decrease in diacyl PC lipids may be a general characteristic of peroxisomal disease samples. Overall, these results show that the tight regulation of overall PE levels, and thus the upregulation of diacyl PEs in Pex7 deficient mice, occurs for specific brain regions (hippocampus, cortex) – in alignment with previous fibroblast experiments[1] – but not for all tissue types (cerebellum). We additionally observe tissue region-specific trends in up- or downregulation for either 20:4- or 20:6-containing diacyl PEs or PCs.

(1) Schrakamp, G.; Schalkwijk, C. G.; Schutgens, R. B.; Wanders, R. J.; Tager, J. M.; van den Bosch, H. Plasmalogen Biosynthesis in Peroxisomal Disorders: Fatty Alcohol versus Alkylglycerol Precursors. *J. Lipid Res.* **1988**, *29*, 325–334.